Two-layer thermal convection in miscible viscous fluids

By ANNE DAVAILLE

Department of Geology and Geophysics, Yale University, POB 208109 New Haven,
CT 06520-8109, USA and Laboratoire de Dynamique des Systèmes Géologiques, IPG,
4 Place Jussieu, 75252 Paris cedex 05, France

The influence of a viscosity stratification on the interaction between thermal convection and a stable density discontinuity is studied, using laboratory experiments. Initially, two superposed isothermal layers of high-Prandtl-number miscible fluids are suddenly cooled from above and heated from below. By adjusting the concentrations of salt and cellulose, Rayleigh numbers between 300 and 3×10^7 were achieved for density contrasts between 0.45 % and 5 % and viscosity ratios between 1 and 6.4×10^4. Heat and mass transfer through the interface were monitored.

Two-layer convection is observed but a steady state is never obtained since penetrative convection occurs. A new interfacial instability is reported, owing to the nonlinear interaction of the unstable thermal and stable chemical density gradients. As a result, the temperature condition at the interface is highly inhomogeneous, driving, on top of the classical small-scale thermal convection, a large-scale flow in each layer which produces cusps at the interface. Entrainment, driven by viscous coupling between the two layers, proceeds through those cusps. The pattern of entrainment is asymmetric: two-dimensional sheets are dragged into the more viscous layer, while three-dimensional conduits are produced in the less viscous layer. A simple entrainment model is proposed and scaling laws for the entrainment rate are derived; they explain the experimental data well.

1. Introduction

Convection in superimposed layers of fluids with different properties is a common occurrence both in industry (e.g. in chemical reactors) and nature (e.g. ocean, atmosphere, magma chambers, and mantle). One of the major unsolved problems in geophysics is whether convection in the Earth's mantle occurs in two distinct layers or extends throughout the mantle. Current work in the earth sciences aims at synthesizing various (and often conflicting) lines of evidence from geochemistry, seismology, and geodynamics (Olson, Silver & Carlson 1990). Besides the pattern of convection, one of the fundamental, and most controversial, questions concerns the rate of mass transfer across the boundary at 670 km depth between the upper and lower mantle. Since the mantle is extremely viscous, inertia is negligible compared to viscous forces and the typical lengthscale of convection is hundreds or thousands of kilometres. Therefore, two questions arise: 'Can thermal convection drive entrainment at the interface between two laminar, viscous fluids?' and 'How does entrainment interact with the dynamics of two-layer thermal convection?' To understand the dynamics of such a system, we thus need to investigate the interaction of thermal convection

in a 'two-layer Bénard problem' with a stable density gradient, using fluids that are viscous and miscible (i.e, with no surface tension effects).

Thermal convection in superposed fluid layers with different properties has been extensively investigated (see Joseph & Renardy (1993) for a review), but few of these studies have examined the entrainment dynamics. Early work used linear stability analysis to investigate the stability of various two-layer systems as a function of Rayleigh number and density contrast (Richter & Johnson 1974; Busse 1981; Ellsworth & Schubert 1988; Sotin & Parmentier 1989). The presence of a deformable interface offers the possibility of Hopf bifurcations: since it introduces an additional degree of freedom, overstability can occur in the form of oscillatory interfacial instability (Richter & Johnson 1974; Renardy & Joseph 1985*a, b*; Renardy & Renardy 1985; Rasenat, Busse & Rehberg 1989). Numerical studies of two-layer convection at finite amplitude have typically focused on the mechanism of coupling (thermal *vs.* mechanical) between the layers, often treating the interface as impermeable (Christensen 1980; Richter & McKenzie 1981; Kenyon & Turcotte 1983; Christensen & Yuen 1984; Cserepes & Rabinowicz 1985; Boss & Sacks 1986; Cserepes, Rabinowicz & Rosemberg-Borot 1988).

Highly nonlinear convective regimes, due to high Rayleigh numbers or entrainment at the interface, are not easily accessible to theoretical or numerical studies. However, two-layer convection in highly viscous fluids can also be studied experimentally. Using aqueous glycerol solutions, Richter & McKenzie (1981) showed that two-layer convection is stable when the ratio of chemical to thermal buoyancy R_ρ exceeds unity, but they did not address the issue of partial mixing. Olson (1984) used aqueous sugar solutions to study two-layer convection in the penetrative regime $R_\rho = 1$, when the viscosity ratio between the two layers is lower than 10. His results established that entrainment at low Reynolds number can indeed occur, and that viscous stresses can substitute for inertial instabilities as a mixing mechanism. Nataf, Moreno & Cardin (1988) demonstrated that the mechanism of coupling between immiscible fluid layers depends on conditions at the interface (e.g. surface tension, impurities), and that the oscillatory interfacial mode is stabilized by surface tension, as predicted by theory. Indeed, the oscillatory interfacial mode has never been reported experimentally. This indicates one shortcoming of experimental studies: it is not possible to obtain a 'clean' interfacial condition of zero surface tension, especially when other properties of the fluids, like the viscosities, are very different. Either the experimental fluids are immiscible, or they are miscible and some diffusion of material occurs across the interface. This latter case of double-diffusive convection has been extensively studied for iso-viscous and low-viscosity fluids, motivated mostly by ocean and atmosphere dynamics and industrial applications such as crystal growth and solar ponds (for reviews, see, for example, Turner 1979; Fernando 1991; Schmitt 1994).

Despite this wealth of studies, the parameter space of two-layer convection (physical property ratios plus the Rayleigh and Prandtl numbers characterizing classical one-layer Rayleigh–Bénard convection) is so large that the parameter range likely to be relevant to the mantle has not been fully investigated. I have thus focused on the interaction of thermal convection with a discontinuity in density and viscosity. Using a new experimental technique (Tait & Jaupart 1989), I was able to change the viscosity ratio by up to 6×10^4 while maintaining effectively zero surface tension at the interface. The aims of these laboratory experiments are to provide a set of data on penetrative two-layer convection from moderate to high Rayleigh numbers and viscosity ratios, to propose a mechanism to explain them, and to determine scaling laws to predict heat and mass transfer.

The plan of this paper is as follows: the apparatus and experimental methods are described in §2. Section 3 is devoted to a general description of the evolution of the fluid layers. In §4, a mechanism for entrainment is proposed and scaling laws for the variables of interest are derived and verified against the experimental data.

2. Experimental set-up

2.1. *Apparatus and working fluids*

A Plexiglas tank was built, 15 cm high and 35 cm × 35 cm in horizontal dimension with 3 cm thick walls. The upper and lower boundaries are copper plates through which temperature-controlled water circulates. The tank and copper plates were covered with styrofoam plates 4 cm thick to minimize heat losses.

The working fluid was water, to which small amounts of salt and cellulose (trade name Natrosol) were added to control the density and the viscosity, respectively. Using this technique, due to Tait & Jaupart (1989), viscosity variations of up to 10^5 can be obtained by adding less than 2 % Natrosol to the solution (Appendix A), without affecting the other physical properties of the salted water except the chemical diffusion of salt. For the low deformation rates associated with the velocity of convective features in the tank, the solutions always remain Newtonian (Appendix A).

This technique has four important advantages: (i) it allows the viscosity and the density to be varied independently; (ii) the solutions used for the two layers are totally miscible, eliminating the unwanted effect of surface tension at the interface; (iii) adding Natrosol increases the Prandtl number Pr of the solution, so that one can always work in the viscosity dominated regime, i.e. $Pr \geqslant 100$ (Krishnamurti 1970); and (iv) the viscosity of the salt–cellulose solution is a relatively weak function of temperature (Tait & Jaupart 1989), which facilitates the interpretation of the results.

The density and viscosity of the fluids used for each experiment were measured in the laboratory. All the relevant physical properties are listed in Appendix A. One of the layers was dyed (using food dye) to allow better visualization of mixing and movement of the interface.

2.2. *Experimental conditions*

Filling the tank was difficult; a well-controlled experiment required the absence of bubbles and minimal mixing when the upper layer was introduced on top of the lower layer. Thus, the most viscous layer was usually introduced first, and left several days to rest and degas. The less viscous layer was then introduced slowly from the top. The aspect ratio in a single layer of fluid varies between six (at the beginning of an experiment when two layers coexist, see table 1) and two (at the end of an experiment, when only one layer remains in the tank since the two fluids have been completely mixed, see below). However, for high Rayleigh numbers, the relevant aspect ratio is that of the width of the tank to the thickness of the unstable boundary layer, which typically has a value of 20.

Initially, the two well-homogenized layers are at the same temperature, so that the vertical profiles of density and viscosity are step functions. The most viscous layer was nearly always at the bottom of the tank (except in two cases, see table 1). At $t = 0$, both baths are turned on, and the lower (upper) copper plate is continuously heated (cooled) until the bath has reached its assigned temperature T_1 (T_2). The thermal boundary conditions at the upper and lower plates were thus close to 'fixed heat flux' for typically 30 min and 'fixed temperature' afterwards. Accordingly, convection often

Number	Type	γ	Pr_1	Ra_1	Ra_2	$R_{\rho 1}$	$R_{\rho 2}$	$\Delta\rho/\rho$ (%)	ΔT (°C)	T_2 (°C)	χ	t_{diff} (hours)
4.10	M	10^{-1}	92	2.9×10^7	1.0×10^5	0.97	24.0	2.00	34.3	4.7	1.03	1.15
4.20	M	25	1500	1.1×10^6	1.6×10^6	1.31	27.2	1.80	34.0	5.0	1.03	12.0
4.30	M	27	1500	1.1×10^6	1.7×10^6	1.53	27.2	2.10	33.9	5.0	1.00	2.0
4.40	M	21	1910	5.4×10^5	7.3×10^5	2.33	34.7	1.95	24.7	5.0	1.00	3.0
4.50	M	297	2.7×10^4	6.2×10^4	1.0×10^6	1.69	30.3	2.35	34.1	5.0	1.00	3.0
4.60	M	17	1530	1.2×10^6	9.6×10^5	2.38	43.4	3.35	33.9	5.0	1.03	2.0
4.70	M	65	5980	3.3×10^5	8.5×10^5	1.64	29.4	2.28	34.0	5.0	1.11	1.5
7.10	M	54	2.9×10^4	9.1×10^4	1.9×10^5	1.41	32.8	2.90	43.8	4.8	1.03	1.45
7.20	M	129	3.1×10^4	8.6×10^4	4.1×10^5	1.22	29.2	2.50	43.95	4.75	1.03	0.45
7.30	M	226	3.1×10^4	9.8×10^4	7.6×10^5	1.18	26.4	2.60	45.90	4.9	1.08	0.45
7.40	M	300	3.5×10^4	5.4×10^4	6.4×10^6	1.61	3.97	2.50	32.1	19.4	1.00	1.0
8.00	NS	4×10^4	2.2×10^5	1.4×10^4	3.6×10^6	0.191	2.67	0.45	48.8	5.9	1.03	14.0
8.10	M	85	1.4×10^4	2.2×10^5	9.9×10^5	0.82	15.2	2.00	49.3	5.3	1.00	1.5
8.20	M	85	1.3×10^4	2.2×10^5	9.3×10^5	1.35	28.1	3.35	49.5	5.1	0.97	1.5
8.30	M	90	1.4×10^4	2.2×10^5	8.0×10^5	1.89	45.0	4.80	49.7	4.9	1.00	2.0
8.40	M	1.04	2050	2.3×10^5	2.3×10^5	2.52	19.2	3.10	30.05	7.4	0.51	2.5
8.50	M	6.4×10^4	1.1×10^7	300	4.1×10^5	1.25	51.3	3.15	50.4	4.2	1.03	1.5
8.60	M	1336	2.0×10^5	1.6×10^4	5.6×10^5	0.97	32.4	2.40	49.95	4.4	1.03	1.5
8.70	M	368	6.7×10^4	4.7×10^4	4.7×10^5	0.93	31.1	2.30	49.9	4.4	1.03	2.0
8.80	M	381	4.6×10^4	6.8×10^4	8.3×10^5	0.92	26.0	2.25	49.5	4.6	1.03	1.0
8.90	M	480	6.5×10^4	2.8×10^4	5.9×10^5	1.67	34.0	2.35	34.3	4.8	1.03	1.5
9.10	M	25	4050	7.4×10^5	6.4×10^5	0.94	24.2	2.20	48.3	4.7	1.03	0.45
9.20	M	50	4050	3.0×10^5	3.0×10^6	0.97	27.0	2.30	48.7	4.6	0.59	2.0
9.50	SR	30	4050	7.0×10^5	1.1×10^6	1.01	18.5	2.35	47.6	5.3	1.00	
9.60	SR	30	4050	7.0×10^5	1.1×10^6	1.01	18.5	2.35	47.6	5.3	1.00	

TABLE 1. List of experiments: SR denotes the presence of Saran wrap which inhibits the mixing at the interface, M the presence of mixing at the interface, and NS an experiment where the density contrast is due only to the natrosol content. In this latter case, mixing occurs as well.

started in the layers when the system was still in the fixed heat flux regime. However, I was primarily interested in the quasi-stationary regime of convection that obtained once the fixed temperature condition was attained.

A danger was that the system dynamics would depend highly on the initial state of the interface, namely the exact interfacial density profile due to the molecular diffusion of salt through time. To check this, two experiments were duplicated: the dimensionless parameters were identical but, prior to the start of the cooling and heating, the interface was allowed to diffuse for two hours in one case, and for one night in the other (table 1, runs 4.20 and 4.30). The subsequent behaviour of the system turned out to show no differences in the long run.

Two other experiments were conducted where chemical transfer at the interface was mechanically inhibited by a plastic film 0.1 mm thick (Saran wrap). Otherwise, the interface could deform and the heat transfer properties remained unchanged. Those experiments were designed to evaluate the influence of chemical entrainment on the thermal regime of the system, i.e. the importance of the coupling between the chemical stable density gradient and the thermal unstable density gradient (table 1, runs 9.50 and 9.60).

The variables characterizing the system are the temperature difference applied to its boundaries $\Delta T = T_1 - T_2$, the depth of the lower layer h and the total depth of the tank H, the thermal diffusivity κ, and chemical diffusivity of salt D, the densities ρ_i and the viscosities v_i of the respective layers at $23\,^\circ$C, the coefficients of thermal expansion α_i, where the index i is the number of the layer considered (lower layer is 1 and upper layer is 2). The thermal diffusivity is supposed to be independent of temperature and salinity, and it does not depend on the Natrosol content (S. Tait, private communication). The salt diffusivity, however, depends on the Natrosol content, mainly because its mobility is greatly reduced when the viscosity increases (see Appendix A). The variation of viscosity with temperature (less than factor 2, see Tait & Jaupart 1989) is neglected, compared to its variation between the two layers. The coefficients of thermal expansion depend strongly on temperature (Ruddick & Shirtcliffe 1979) and therefore to obtain a meaningful value α_i in each layer is difficult. However, we expect the convection in each layer to be partly, if not mainly, driven by the boundary-layer instabilities at its solid boundary, i.e. by the buoyancy available at temperature T_i (cf. Appendix B). Unless otherwise stated, α_i is thus calculated at temperature T_i and the salinity of layer i. The diffusivities of Natrosol and dye were considered to be zero. According to the Buckingam–Pi theorem, there are therefore seven independent dimensionless parameters characterizing the dynamics of the system:

$$Le = \frac{D}{\kappa}, \tag{1a}$$

$$Pr_i = \frac{v_i}{\kappa} \quad (i = 1, 2), \tag{1b}$$

$$Ra_1 = \frac{\alpha_1 g \Delta T h^3}{\kappa v_1}, \tag{1c}$$

$$Ra_2 = \frac{\alpha_2 g \Delta T (H - h)^3}{\kappa v_2}, \tag{1d}$$

$$R_{\rho i} = \frac{\rho_1 - \rho_2}{\alpha_i \Delta T \rho} = \frac{\Delta \rho}{\alpha_i \Delta T \rho_i} \quad (i = 1, 2). \tag{1e}$$

Two other useful parameters are obtained from the combination of the dimensionless

Type	Depth (cm)
Thermocouples	0 (bottom plate), 0.50, 1.05, 2.20, 3.00, 5.00, 7.05, 8.10, 8.70
	9.15, 10.50, 12.10, 12.95, 14.15, 14.65, 14.80 (top plate)

TABLE 2. Depth coordinates of thermocouples. These coordinates correspond to experiments 4.50 to 4.70 only, as the positions of the probes were changed between series of experiments.

groups:

$$\gamma = \frac{v_1}{v_2} \quad \text{viscosity ratio,} \tag{2a}$$

$$\chi = \frac{h}{H - h} \quad \text{layer depth ratio.} \tag{2b}$$

The experiments are listed in table 1. Twenty-six 'clean' experiments were conducted with characteristic duration ranging from 1 day to 2 weeks. In most cases, the two layers had the same depth initially. By adjusting the concentrations of salt and cellulose and the temperatures of the boundaries, we obtained initial Rayleigh numbers Ra_1 and Ra_2 between 300 and 3×10^7 with initial density contrasts between 0.45 % and 5 %, viscosity ratios between 1 and 6.4×10^4, and thermal expansion ratios between 2 and 45. The Prandtl number was always greater than 90. However, each experiment spans a larger range of dynamics than might be expected. During an experiment, the two layers of fluid mix slowly, so that the density contrast, viscosity ratio and chemical and thermal structures of the tank evolve through time. At each given time, one may calculate effective values of the Rayleigh number using the instantaneous values of temperature difference, depth of the layer and interior density and viscosity. Effective Rayleigh numbers calculated in this way ranged from about 300 to 5×10^7.

2.3. *Measurements*

Temperature

A set of 14 thermocouples was used to measure local temperature at selected points, mostly located in the boundary layers. Table 2 lists the coordinates of all these probes. Thermocouples were also placed in the lower and the upper plates. All temperatures were read every 30 s through a scanning voltmeter connected to a computer.

The 14 thermocouples were divided into two vertical probes of 7 thermocouples each (cf. Guillou & Jaupart 1995). These probes have a 2 mm diameter and give temperature with an accuracy of $\pm 0.025\,°C$ at depths known to within ± 0.2 mm. Their response time is about 2 s, much shorter than the period of fluctuations in these experiments (typically several minutes). The measurements exhibit large fluctuations which record the passage of thermal structures like plumes (figure 1), superimposed on a long-term trend. The latter was fitted by a polynomial, and temperature fluctuations were then determined by removing this long-term component from the readings.

The probes were designed to be much smaller than the dimensions of the convective features, so as not to perturb the flow significantly. By moving around the temperature probes, I verified that no convective motion was preferentially localized in their vicinity. Although temperatures in an experiment steadily evolve with time, at sufficiently high Rayleigh numbers one expects quasi-ergodic conditions, such that time and spatial averages are locally equivalent. Indeed, in the experiments without
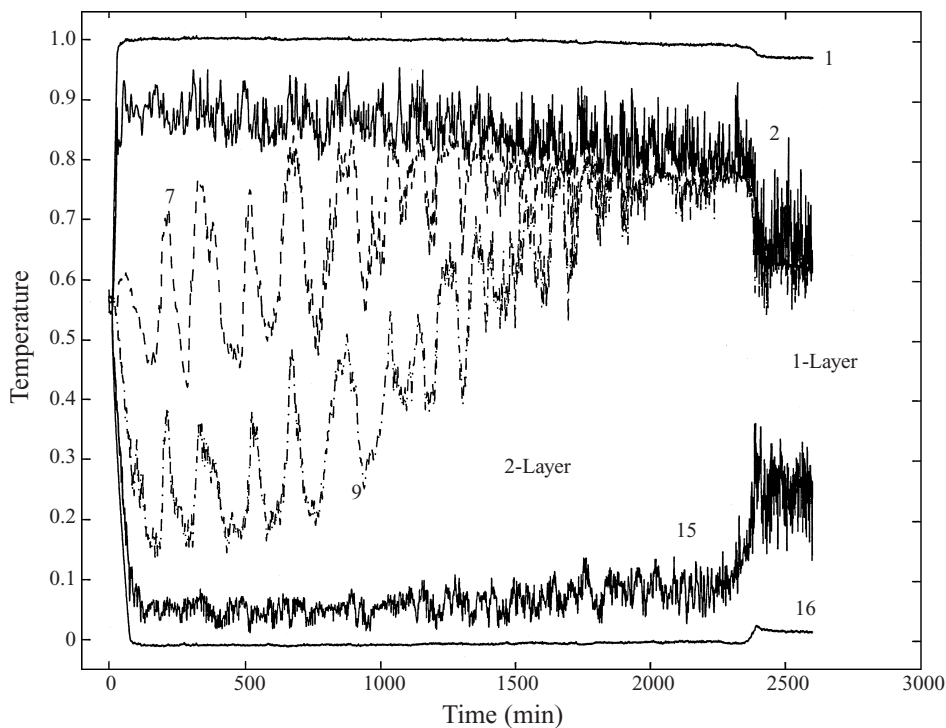
FIGURE 1. Time evolution of the local temperature measured by six of the thermocouples in experiment 4.60. After a short transient, the copper plates (thermocouples 1 and 16) are regulated at constant temperature. Thermocouples 2 and 15 are localized into the thermal boundary layers close to the copper plates. Thermocouples 7 and 9 are situated initially around the interface.

entrainment, the smoothed time series from 2 thermocouples on the same horizontal plane, but at different locations, gave the same values. However, in experiments where entrainment took place, ergodicity did not obtain.

Mixing

Periodically, small samples of fluid (typically 10 ml) were removed at different known depths with a syringe. The removal was slow enough (about 10 s) not to disturb the flow but still rapid compared to the characteristic timescale of the convective features.

This periodic sampling made it possible to follow the evolution of the density of the two layers through time, using two different techniques. First, the salinity of each sample was measured, using the dependence of the refractive index on the salt concentration. Then the dye concentration was measured using a UV absorption technique. These two techniques suppose that refractive index and UV absorption are sensitive only to salt and dye, respectively, whereas both layers also contain Natrosol. Accordingly, before each experiment samples of known mixtures of layers (1) and (2) were made and a calibration curve measured for both techniques, giving the density as a function of refractive index or UV absorption. For all the experiments, the calibrations exhibit a linear behaviour. With this technique, the precision of the density measurements is $\pm 1\,\mathrm{g\,l^{-1}}$, about 5 % of the total density contrast.

The dye diffuses at least ten times more slowly than the salt. So, if both measurements give the same value of the density, this proves that entrainment and mixing at the interface is controlled mainly by advection, not diffusion. In this case, one can

A. Davaille
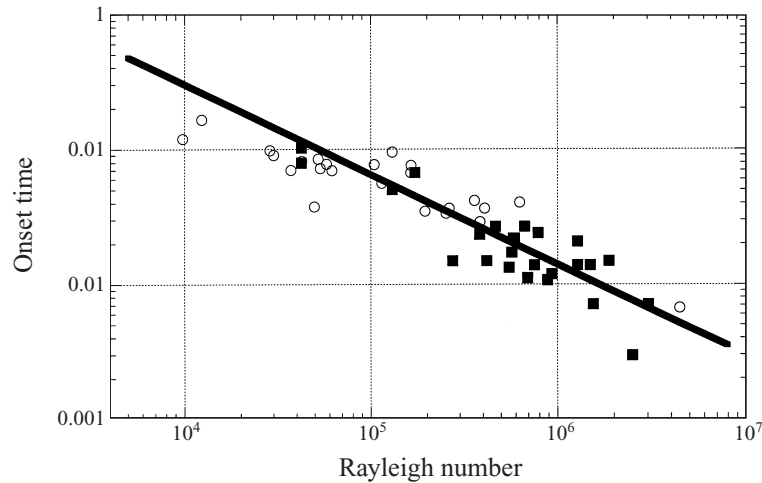
FIGURE 2. Critical time of the onset of convection in each of the layers divided by the thermal diffusion time as a function of the Rayleigh number. ○, lower layer, ■, upper layer. The slope of the solid line is $-\frac{2}{3}$.

assume that the Natrosol was also entrained at the same rate, and therefore calculate the respective viscosities of the two layers at any time from their respective densities.

The deformation and migration of the interface, as well as the convective patterns were visualized either directly or by shadowgraph.

3. The characteristics of convection

3.1. *Onset of convection and mixing*

Onset of thermal instability

At the onset, convective motions take the form of downgoing plumes generated at the upper boundary and/or upgoing plumes generated at the lower boundary. The typical lengthscale of these instabilities is 1–3 cm. For layers of equal thickness, convective instabilities always appeared in the less viscous (generally upper) layer first.

From the temperature profiles, the onset of instability can be defined as the time at which temperature at a fixed depth deviates from the initial conductive cooling or heating trend by $\Delta T/10^2$ (Davaille & Jaupart 1993). With this method, the critical time for the onset of convective instabilities is determined with an error of ± 15 s, i.e. between two successive temperature scans. In all cases, the onset of instability was very sharp and is recorded simultaneously at all depths in the boundary layer. Below or above the boundary layers, the temperature stays constant until the arrival of convective plumes. The measured onset times range between 2 and 45 min. The local timescale for boundary-layer instabilities at high Rayleigh numbers can be evaluated for each separate layer and should scale as (Howard 1964; Blair & Quinn 1969; Kaviany 1980; Davaille & Jaupart 1994):

$$\tau_b = \frac{h^2}{\kappa} \left(\frac{Ra_c}{Ra_i} \right)^{2/3}, \tag{3}$$

where Ra_c is the critical Rayleigh number and Ra_i the instantaneous Rayleigh number of layer i. Since during the onset of convection, the copper plate temperature condi-
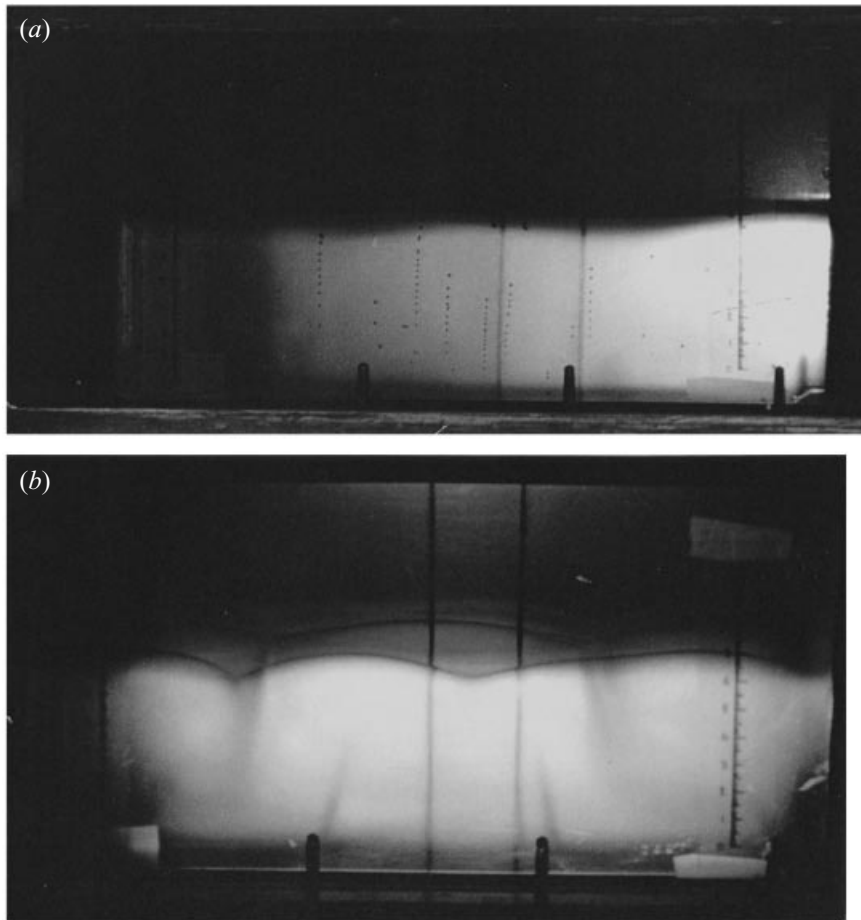
FIGURE 3. Snapshots of the entrainment pattern (run 8.60). (*a*) onset of the interfacial instability: note the undulation of the interface. Thermal convection was already fully developed in both layers. (*b*) 15 min later: in the lower-most viscous layer, the undulation has degenerated into cusps, forming a pattern of nine approximately square cells.

tions were somewhere between 'fixed flux' and 'constant temperature', the Rayleigh number is based on the difference between the real plate temperature at the onset of convection and the initial homogeneous temperature of the fluid. Therefore, the characteristic timescale (equation (3)) is a lower bound. Figure 2 shows the dependence of the measured onset time on the Rayleigh number. Despite a large scatter (due, for $Ra > 10^5$, to the imperfect temperature boundary condition), the trend is compatible with equation (3). The best fit of a law in $Ra_i^{-2/3}$ gives a critical Rayleigh number of 1641 ± 422, close to the theoretical value of 1100.65 for the onset of convection between one solid and one free boundary (Pellew & Southwell 1940). In the range of Rayleigh numbers studied here, the two boundary layers located near the copper plates seem thus completely uncorrelated.

Onset of mixing through interfacial instability

The onset of any visible entrainment in one layer occurs typically two hours after the beginning of the experiment, i.e. much later than the onset of thermal instability
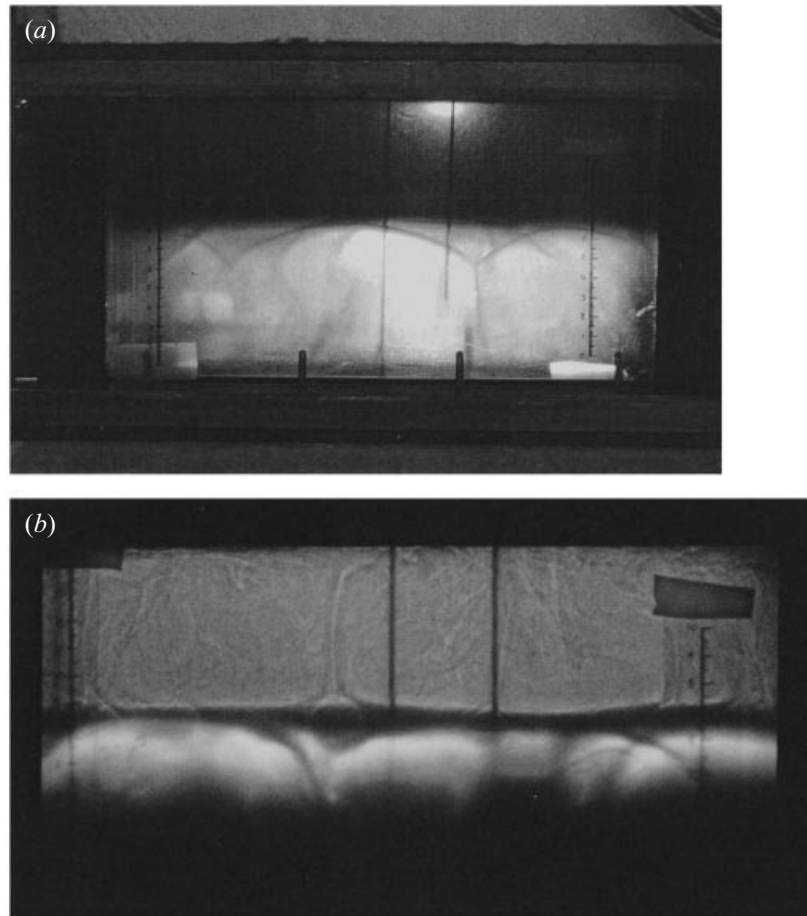
FIGURE 4. Run 8.60. 240 min after the onset of convection. (*a*) Direct view of the entrainment in the more viscous layer. The interface remains flat and sharp. Cusps are formed through which thin schlieren of light, low-viscosity fluid are entrained. (*b*) Shadowgraph. Although most of the lower layer has been masked, one can distinguish three or four cells. In the upper layer, note the very thin conduit originating at the interface (centred on top of a cell unfortunately in the background) and not distorted until it encounters the upper cold thermal boundary layer.

and after convection is fully developed in at least one layer. First, the interface, initially flat, suddenly develops an undulation with an amplitude of a few millimetres, and a typical wavelength of 10 cm (figure 3 *a*). Within 5 to 10 minutes, the extremum of the undulation in the most viscous layer becomes unstable and develops a cusp (figures 3 *b* and 4 *a*) and tendrils of the less viscous layer are entrained in the more viscous layer. In the absence of surface tension, it has been shown theoretically that it is a true cusp (Lister 1989; Joseph *et al.* 1991; Jeong & Moffatt 1992). Entrainment proceeds only through these cusps (figure 4). Similar entrainment features have been observed in crystallizing experiments at the bottom of a viscous fluid where the released material, less viscous and less dense, was coming through the upper layer in thin tendrils (Huppert, Sparks & Turner 1984). The instability of the interface and the subsequent entrainment of material creates a large-scale, square pattern with typically nine cells in the tank (figure 3 *b*) when both layers have initially the same depth (7.4 cm), irrespective of the amount of time (between 2 and 12 hours) the interface

has been allowed to diffuse before starting the experiment. The wavelength of this pattern (10 cm) is quite different from that of the thermal instabilities (1–2 cm) in either convecting layer, and does not show a strong dependence on the viscosities or the Rayleigh numbers. Moreover, in run 8.50, cusps appeared and less dense material (the buoyancy ratio was at the interface >10) was entrained downwards in the lower more viscous layer even though its thermal Rayleigh number was subcritical: if due solely to classical Rayleigh–Bénard convection, no motion should have occurred (table 1).

In summary, whereas the initial instability of the system is always a 'single fluid' mode, comprising convective thermal instabilities in one or both of the fluids (depending on the respective Rayleigh numbers of the layers), the onset of entrainment proceeds from a distinct interfacial mode.

3.2. *Convection and mixing in the fully developed regime*

Except when mixing was mechanically prevented by the presence of Saran-wrap film, a steady state was never attained in the two-layer configuration. Instead, one observes penetrative convection across a more or less distorted interface. The lower the density contrast and the greater the viscosity ratio, the greater is the deformation of the interface. For density contrasts greater than 2 %, the interface remains sharp and 'flat' (within 1 mm) for the duration of an experiment.

In the presence of a viscosity contrast, each layer incorporates thin tendrils of the other, but with different spatial patterns and therefore with different rates. Entrainment in the most viscous layer occurs only in the form of two-dimensional sheets that form a large-scale three-dimensional pattern of rectangular cells (figure 3 *b*). Although the cells exhibit slow spatial oscillations during the course of an experiment, their wavelength changes little (figures 4 and 5). In the less viscous layer, entrainment occurs through very thin (1–2 mm in diameter) steady tubular plumes that are centred on each of the former rectangular cells (figure 4 *b*). The timescale of these cylindrical plumes depends on the timescale of those cells, and is thus much longer than the characteristic timescale of boundary-layer thermal instabilities. This asymmetrical configuration is seen regardless of whether the more viscous layer is above or below. The entrainment features (sheets or cylindrical plumes) extend generally over the full depth of each layer. More complete mixing then proceeds through folding of the entrained schlieren by small-scale thermal convection and ultimately molecular chemical diffusion.

The asymmetry of the entrainment pattern also produces an asymmetry of the fluxes of material entrained in each layer across the interface, entrainment of less viscous fluid into the more viscous layer being the most efficient as will be seen further on. Hence, a lower, more viscous layer which convects always ends up growing at the expense of the upper, less viscous layer. The interface moves steadily upward (figures 4 and 5) until it reaches the top boundary, and no catastrophic overturn occurs. It was unfortunately impossible to observe the same behaviour when the more viscous layer (containing initially more Natrosol and no salt) was the upper layer (run 4.10) because our three-component system (water, salt, Natrosol) then developed salt/Natrosol fingers at the interface. Although the large-scale pattern of the thermochemical mode at later stages looked the same as previously described (three-dimensional downgoing plumes in the less viscous layer and two-dimensional upgoing sheets in the more viscous layer), the dynamics of the system were much more sluggish and the interface rose very slowly. This run will thus not be further considered. Nevertheless, in this and all other configurations investigated here, the
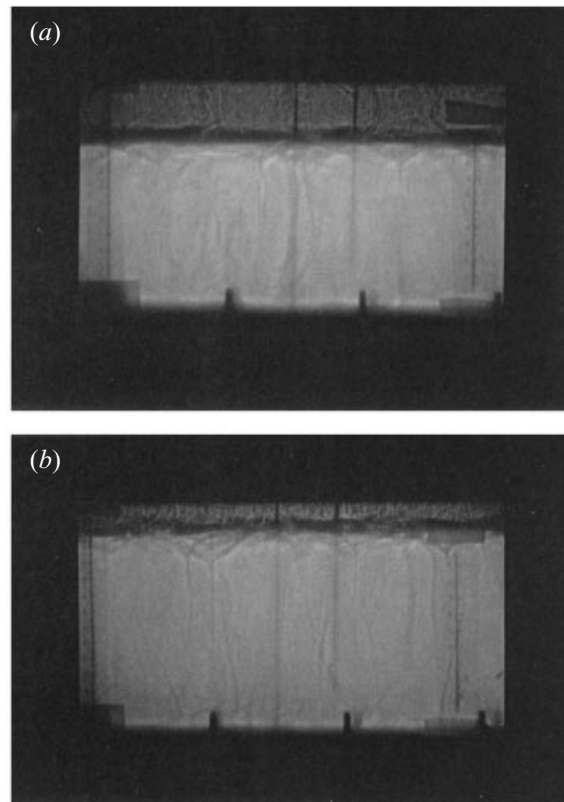
FIGURE 5. Run 8.60. (*a*) Shadowgraph 1320 min after the onset of convection: the interface is still sharp but is moving up. (*b*) 1600 min after the onset of convection: convection still exists in both layers.

final state of the experiments is always thermal convection in a single homogeneous layer. This is the only steady state configuration.

Thermal structure and heat transfer

Figure 6 shows the vertical temperature profile throughout the tank for two different experiments. In the absence of entrainment (figure 6*a*, run 9.60, cf. table 1), the two-layer configuration is steady through time. It presents three thermal boundary layers with high temperature gradients, two near the copper plates and one at the interface, separated by zones of nearly constant temperature (a weak inverse gradient is noticeable). This configuration looks like two classical Rayleigh–Bénard cells on top of one another (e.g. Chu & Goldstein 1965; Deardorff, Willis & Lilly 1969; Jarvis & Peltier 1982; Asaeda & Watanabe 1989). When entrainment is allowed at the interface (figure 6*b*), the instantaneous vertical temperature structure evolves through time. At first, it presents the same structure as when entrainment is prohibited. As time progresses, the intermediate boundary layer rises and then disappears when the mixing has been completed. In the final, steady, one-layer configuration the temperature profile is not symmetric relative to the mean of the boundary temperature as expected for fluids of constant properties. The discrepancy is explained well by the variation of thermal expansion coefficient with temperature (see Appendix B).

Figure 1 shows the evolution through time of the temperature recorded by
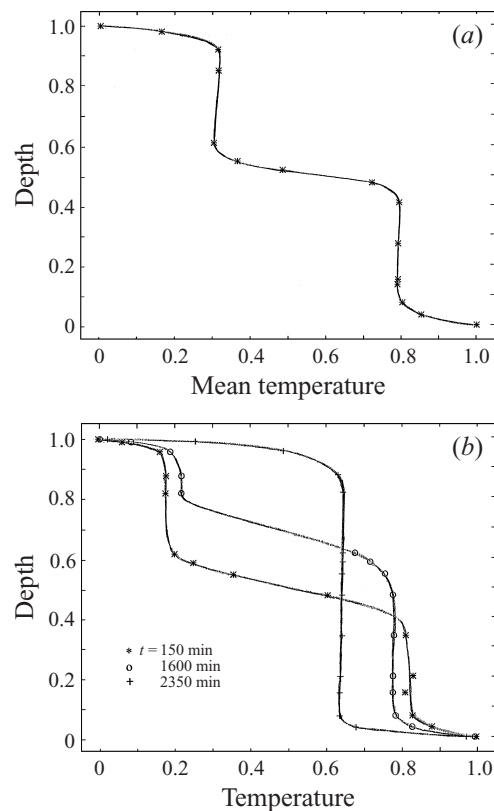
FIGURE 6. Vertical profiles of temperature throughout the tank. (*a*) Experiment 9.60, where entrainment at the interface is not possible. The profile is averaged over 3000 min. The structure is that of the superposition of two classical Rayleigh–Bénard layers, constituted of two zones of high temperature gradient and one core where the temperature is nearly uniform (a weak inverse gradient is noticeable). (*b*) Experiment 4.60, instantaneous profiles for three different times. At the beginning of the experiment, the profile is similar to the previous case (*). Then as entrainment proceeds, the interface moves up (○), and so does the thermal boundary layer associated with it. In the final steady state (+), this intermediate thermal boundary layer disappears completely, and the system exhibits the classical one-layer Rayleigh–Bénard convection structure.

thermocouples at several fixed depths in the tank, and figure 7 the corresponding power spectra of the temperature fluctuations. Three different timescales appear immediately:

(i) Throughout the two-layer regime, there is continuous rise of the temperature of the thermocouples near the interface, owing to their progressive entry into the warmer lower layer as the interface rises. The transition to the final one-layer regime is abrupt and is seen not only on the measurements inside the fluid but also on the temperature records of the two copper plates: the difference in heat transfer between the two regimes is substantial (typically a factor of two, see below) and the two regulating baths are not powerful enough to overcome it. They therefore fail to keep the temperatures of the plates truly constant when the convective regime changes. This weakness of the equipment provides a way to determine the end of the two-layer regime.

(ii) Temperature fluctuations with short periods (5–20 min) occur located in each thermal boundary layer of the layers, corresponding to purely thermal modes. Indeed,
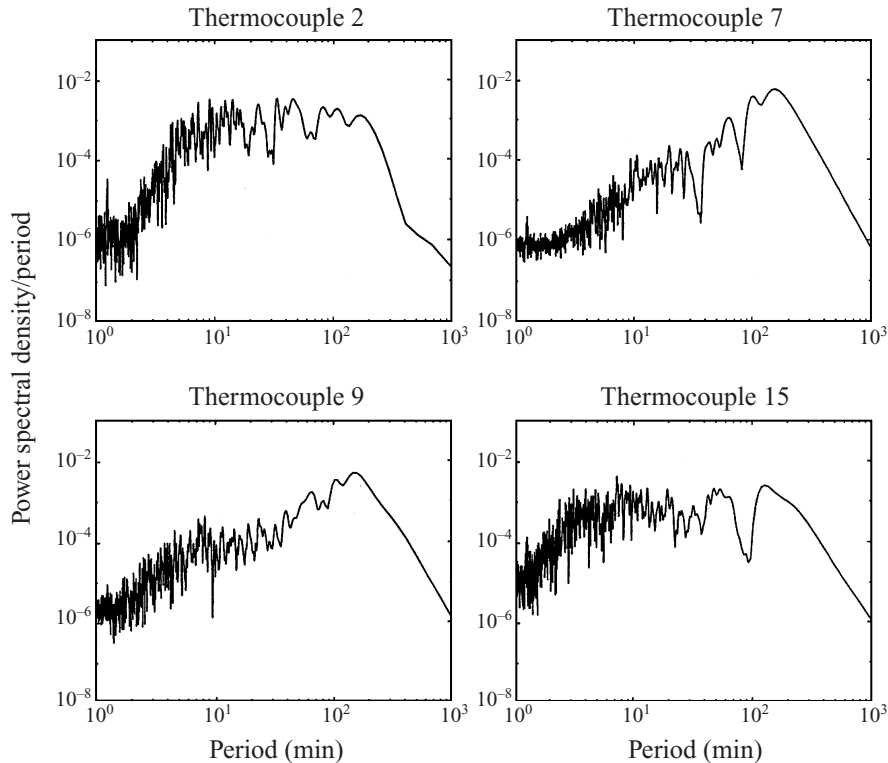
FIGURE 7. Power spectral density of the temperature fluctuations recorded by the thermocouples of figure 1 as a function of the period of the fluctuations (in min). The spectral density has been divided by the period, in order to bring out the lower periods. The thermocouples in the external thermal boundary layers (2 and 15) present a spectrum rich in small periods, while the thermocouples around the interface (7 and 9) exhibit a peak around a period of 150 min (run 4.60).

those fluctuations can be related visually to small thermal boundary-layer instabilities (plumes). They are completely uncorrelated throughout the tank and their amplitude is small ($< \Delta T/10$).

(iii) Long period (> 100 min) temperature fluctuations extend over the whole depth with maximum amplitude at the interface. This maximum amplitude is large, proportional to the temperature difference applied to the copper plates (mean value of $[0.38 \pm 0.06] \times \Delta T$ for all experiments) and shows no clear dependence on the Rayleigh numbers or density difference of the layers (figure 8). These fluctuations are registered with a delay in time by two thermocouples at the same depth but different horizontal positions and correspond visually to the passage of cold downgoing currents (cusps) across the thermocouples. So, the strong lateral heterogeneity of temperature is correlated with the lateral chemical heterogeneity induced by entrainment; and these thermochemical heterogeneities travel along the interface. These fluctuations do not exist when entrainment is inhibited by Saran-wrap film at the interface, even though the interface can still deform and the heat transfer properties are not modified (figure 9). Therefore, these large-amplitude fluctuations are not the result of nonlinear interaction between purely thermal modes (e.g. Proctor & Jones 1988) or between purely thermal modes and a deformable interface, but are indeed due to the interaction between the stable chemical gradient and the unstable thermal gradient at the interface. Moreover, by imposing a varying temperature condition at
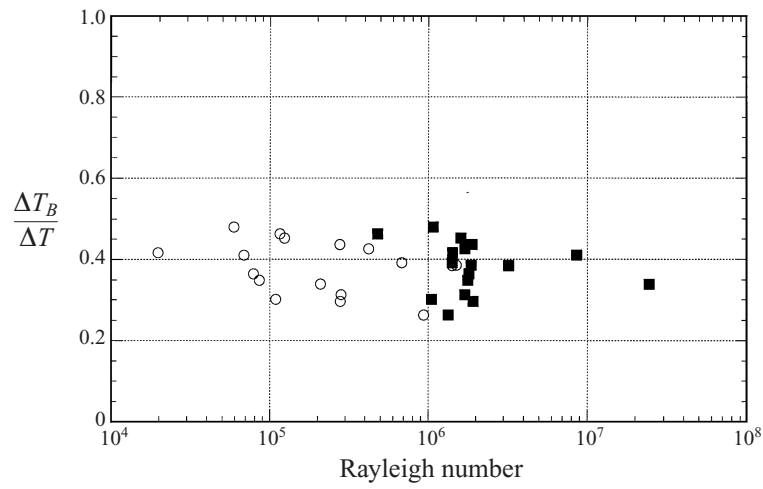
FIGURE 8. 'Thermochemical' signal: amplitude of the interfacial temperature fluctuations as a function of the Rayleigh number. It is approximately constant and scales as $[0.38 \pm 0.06] \times \Delta T$. $\bigcirc$, lower layer, $\blacksquare$, upper layer.
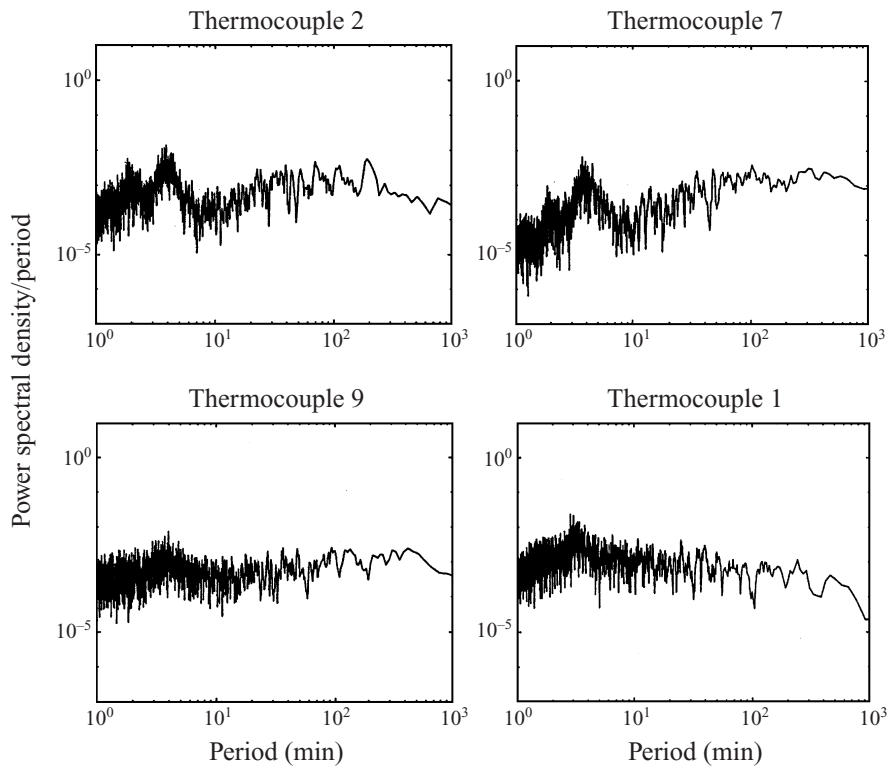

FIGURE 9. Experiment where entrainment at the interface has been prohibited by a film of Saran wrap (run 9.60). Power spectral density of the temperature fluctuations recorded by thermocouples at the same depth as in figure 1. Note the absence of signals of large amplitude and long period.
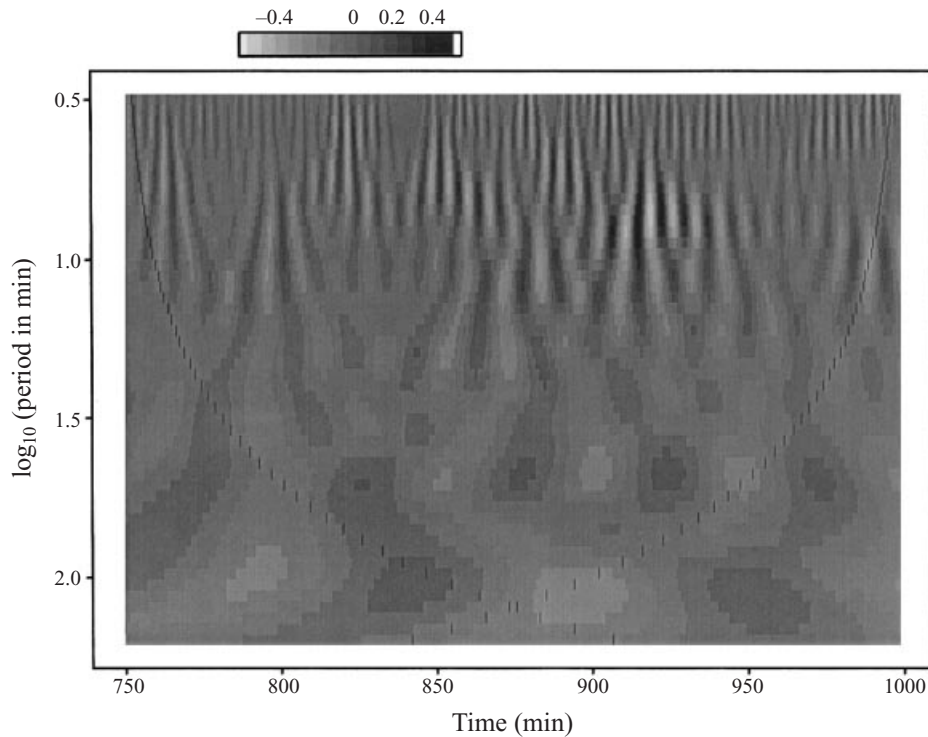
FIGURE 10. Wavelet analysis of the temperature fluctuations recorded by thermocouple 15 of figure 1: the strongest signal is for periods between 5 and 10 min, which is typical of thermal boundary-layer instabilities. However, the exact value is modulated by the weak long-period (around 100 min) signal also present which originates at the interface. In agreement with equation (3), the periodicity of the thermal mode is minimum when the amplitude of the interfacial mode is maximum, i.e. when the interfacial temperature is maximum and convection is most active in the layer.

the interface, this thermo-chemical mode modulates the thermal modes present in the convecting layers. For example, when the temperature difference between the top copper plate and the interface is maximum, convection is most active in the layer, and so according to equation (3), the period of the boundary-layer instabilities is minimum. Indeed, the wavelet analysis of a time series of the temperature within an outer boundary layer (figure 10), shows this modulation of the short period signal by a long period component.

Heat transfer through the lower and upper horizontal copper boundaries can be deduced from the vertical temperature measurements (cf. Appendix B). Figure 11 shows the typical evolution through time of the lower (Q_{s_1}) and upper (Q_{s_2}) heat fluxes. In the one-layer regime at the end of the experiment, the two fluxes are equal and are predicted well by Howard's model (Appendix B). Both fluxes are about twice as high in the one-layer configuration as in the two-layer regime. In the latter, slow oscillations of the fluxes are also recorded in phase with the long period oscillations originating at the interface. Since this large-scale pattern due to entrainment does not change overall but merely oscillates with time, ergodicity no longer obtains: in this regime, the heat fluxes calculated from the temperature measurements on a single vertical line are not entirely representative of the horizontally-averaged heat transfer through the system. Hence, a quantitative scaling law cannot be derived. However, the two fluxes differ systematically and substantially. This can be qualitatively explained
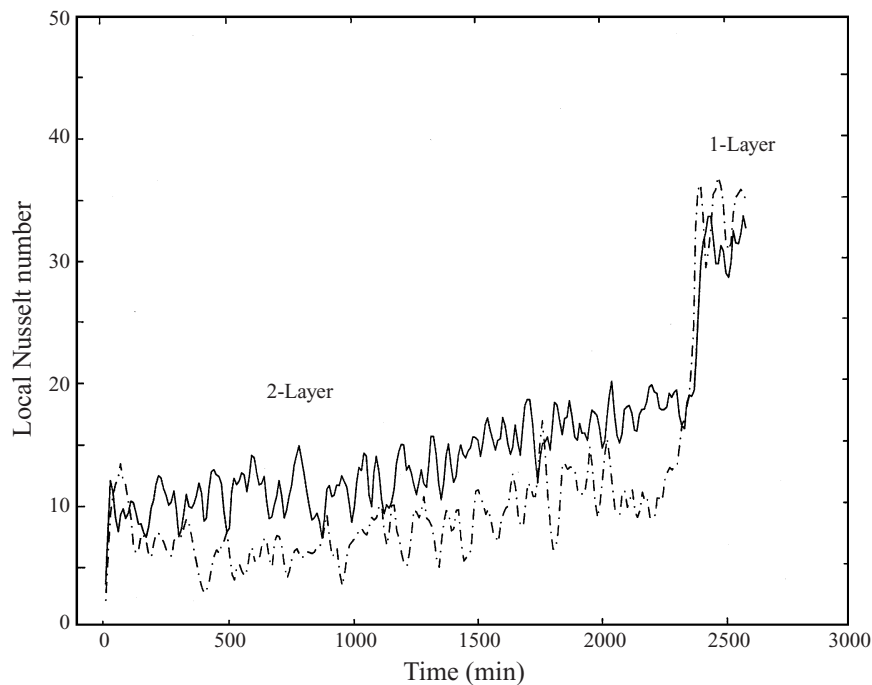
FIGURE 11. Time evolution of the local Nusselt numbers, corresponding to the surface heat fluxes Qs_i normalized by the conductive heat flux through the whole tank $k\Delta T/H$. ——, lower layer, —·—, upper layer.

by considering the horizontal average of the heat equation:

$$\rho_0 C_p \left(\frac{\partial \bar{T}}{\partial t} + \frac{\partial \overline{w\theta}}{\partial z} \right) = \frac{\partial}{\partial z} \left(k \frac{\partial \bar{T}}{\partial z} \right), \tag{4}$$

where k is the thermal conductivity, C_p the thermal capacity, and the horizontal averages are indicated by horizontal bars above the variables. Integrated over the total depth of the tank, this gives:

$$Qs_1 - Qs_2 = k \frac{\partial \bar{T}}{\partial z}(H, t) - k \frac{\partial \bar{T}}{\partial z}(0, t) = \int_0^H \rho_0 C_p \frac{\partial \bar{T}}{\partial t}(z, t) \, dz, \tag{5}$$

since $\rho_0 C_p \overline{w\theta} = 0$ at the rigid boundaries. So, the difference between the upper and lower heat flux is due to the transient nature of the regime, created by the slow mixing between the two layers. Moreover, figure 11 shows that $Qs_1 > Qs_2$ over nearly the whole duration of the two-layer regime, which is consistent with the continuous elevation of the temperatures in the bulk of the fluid owing to the growth of the hotter lower layer (figures 1 and 6).

Chemical structure and mass transfer

As the pattern of entrainment is asymmetrical when the two layers have different viscosities, the interface between the two layers moves through time as shown in figure 12(*a*). However, density cannot be determined only from the interface uplift since the densities in both layers change through time (figure 13). For most experiments, there
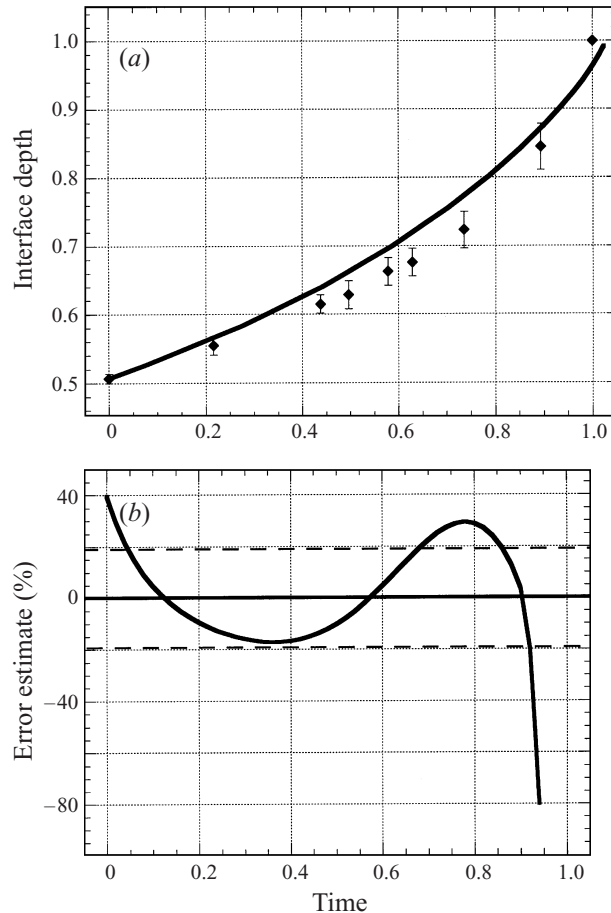
FIGURE 12. Run 9.10. (*a*) Time evolution of the interface depth. Depth has been normalized by H and time by the duration of the experiment t_{end}. (*b*) Closure error of equation (6) as a function of time.

is a good agreement, within the experimental error, between the density measurements based on the salt concentration and on the dye concentration (figure 13), so that salt diffusion is probably negligible.

The sampling method prevented both continuous recording of the density and measurement of the density heterogeneities within one layer. The 'measured density' of each layer thus corresponds to measurements made in the middle of each layer, away from the interface and from the entrainment currents (two-dimensional down-going cold sheets or three-dimensional cylindrical hot plumes). They are supposed to represent an average value of the density in the layer, once mixing (through stretching, folding and molecular diffusion) has taken place. This is, of course, not true in the early stages of an experiment, but becomes valid for the three last quarters of each experiment. In order to get a continuous evolution through time of the interface depth and of the density, each set of data points is fitted by a sum of exponentials.

From the interface and densities measurements, one can calculate the two volume fluxes of material entrained in opposite directions at the interface Q_{12} and Q_{21} (figure
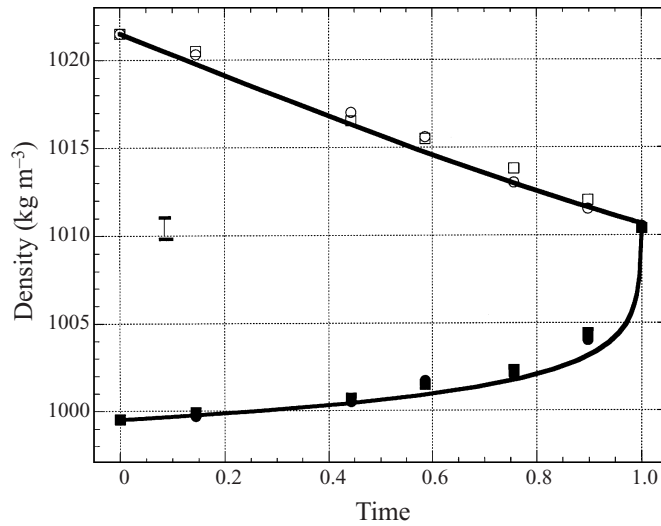
FIGURE 13. Run 9.10. Time evolution of the upper (black symbols) and lower (empty symbols) layers densities, deduced from the salt concentration (squares) and dye concentration (circles) measurements. The two values agree within experimental error. The solid line corresponds to the evolution predicted by the model developed in the text.
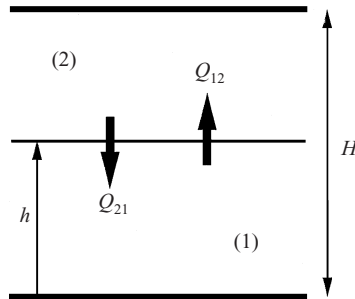

FIGURE 14. Sketch of the global entrainment model. The lower layer is the denser, more viscous layer.

14), using volume and mass conservations in the system:

$$\frac{\partial h}{\partial t} = \frac{1}{L^2}(Q_{21} - Q_{12}), \qquad (6)$$

$$(H - h)\frac{\partial \rho_2}{\partial t} = \frac{\rho_1 - \rho_2}{L^2}Q_{12}, \qquad (7)$$

$$h\frac{\partial \rho_1}{\partial t} = -\frac{\rho_1 - \rho_2}{L^2}Q_{21}. \qquad (8)$$

This method is applicable only if the interface remains sharp (otherwise its position cannot be determined visually) and each layer is well-mixed (otherwise the measured densities ρ_i are not representative of the densities of the layers). However, provided that these conditions are fulfilled, the volume fluxes can be derived directly from equations (7) and (8). However, the scarcity of the density measurements and the difficulty of estimating precisely the depth of the interface (owing mainly to the presence of the cusps) limits the accuracy. Figure 12(*b*) compares the difference of
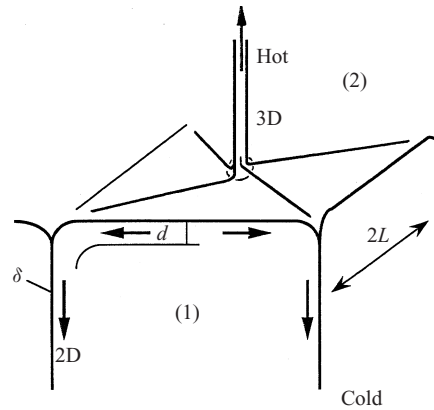
FIGURE 15. Sketch of the asymmetrical laminar extrainment between the two layers,
two-dimensional in the more viscous layer and three-dimensional in the less viscous one.

the calculated fluxes using (7) and (8) and the time derivative of the interface depth derived from the direct depth measurements. It shows that relation (6) holds fairly well except at the begining (when the layers are not yet well mixed) and at the end (when the density difference between the two layers becomes very small) of the experiment. In all that follows, we shall only consider the portions of the experiments where equation (6) holds within 20 %.

4. Two-layer convection and entrainment

Two-layer convection in miscible, but stably stratified, viscous fluids is thus characterized by the superposition of two scales of motion, a small-scale convection driven by the temperature gradient imposed at the copper plates ('thermal mode'), and a large-scale motion originating at the interface and responsible for the entrainment ('thermochemical mode'). Entrainment proceeds through cusps in the interface which remains sharp. The pattern and intensity of entrainment is asymmetrical between the two layers, depending on the viscosity ratio and the Rayleigh numbers. Moreover, the hot (cold) fluid incorporated in the upper (lower) layer is always more (less) dense than that layer, i.e. stable from a density point of view. Finally, even when no thermal mode exists in a layer, the thermochemical mode occurs, and entrainment and motions originate from the interface (run 8.50). This behaviour cannot be reconciled with the existing models of turbulent entrainment in low-Prandtl-number fluids (e.g. encroaching of material by turbulent eddies), or of entrainment in double-diffusive convection (entrainment through a diffusive interface (e.g. Linden & Shirtcliffe 1973; Newell 1984; Fernando 1989)).

4.1. *A mechanistic model of entrainment in laminar fluids*

The entrainment occurs in two steps: first, the thermal heterogeneities at the interface induce circulations in the two layers; then the viscous drag due to those convective motions becomes sufficient to overcome the negative buoyancy forces due to the stable chemical density gradient, and thin tendrils of material are entrained.

Let us assume that the lower layer is the more viscous layer. In the quasi-steady regime, the asymmetric entrainment pattern described in the previous section is summarized by figure 15. The entrainment generated at the interface is correlated with high-amplitude lateral temperature heterogeneities: in the more viscous layer, the

two-dimensional downgoing sheets therefore correspond to cold anomalies, and in the less viscous layer the upgoing cylindrical plumes correspond to hot anomalies. Since the mechanism of entrainment originates at the interface, all the physical properties involved in the following analysis are taken at the temperature of the interface which is approximated well by $\frac{1}{2}(T_1 + T_2)$.

More viscous layer

The horizontal temperature gradient along the interface induces a strong current from the hot zone to the cold zone, and a cold thin downgoing two-dimensional plume (or sheet) is localized below the coldest point. This is similar to the behaviour of convection with non-uniform horizontal heating (e.g. Rossby 1965; Beardsley & Festa 1972). There is no critical Rayleigh number for such a configuration, and the system is always unstable to perturbations. This explains why, even when the Rayleigh number of the layer was subcritical from the point of view of classical Rayleigh–Bénard convection, motion and entrainment were nonetheless observed in the most viscous layer (cf. run 8.50).

One can perform a simple scaling analysis of the two-dimensional system sketched in figure 15. Let ψ be the stream function defined such that the horizontal and vertical component of velocity in Cartesian coordinates can be written respectively as:

$$u = \frac{\partial \psi}{\partial z}, \quad w = -\frac{\partial \psi}{\partial x}. \tag{9}$$

Assuming the Boussinesq approximation for an incompressible fluid, at infinite Prandtl number, the steady-state equations of motion, continuity and energy lead to:

$$\nabla^4 \psi = \alpha g \frac{\partial T}{\partial x}, \tag{10}$$

$$\frac{\partial(\psi, T)}{\partial(x, y)} + \kappa \nabla^2 T = 0. \tag{11}$$

In the interfacial boundary layer, the stream function ψ and the boundary-layer thickness d must be functions of the interfacial horizontal temperature difference ΔT_B. Therefore we take the following scales:

$$x = Lx' \quad \text{where } L \text{ is the half-width of a cell,} \tag{12a}$$

$$z = dz', \tag{12b}$$

$$\psi = \psi_B \psi', \tag{12c}$$

$$T = \Delta T_B T', \tag{12d}$$

where the primes stand for the non-dimensionalized variables. The primed functions and their derivatives in equations (10) and (11) must now be of order unity, which gives (Rossby 1965):

$$\text{boundary width} \quad d = L Ra_B^{-1/5}, \tag{13}$$

$$\text{velocities} \quad U_B \approx \frac{\psi_B}{L} = \frac{\kappa}{L} Ra_B^{2/5}, \tag{14a}$$

$$W_B \approx \frac{\psi_B}{d} = \frac{\kappa}{L} Ra_B^{1/5}, \tag{14b}$$

where Ra_B is here the Rayleigh number based on the interfacial temperature difference

ΔT_B, lengthscale L and viscosity of the lower layer:

$$Ra_B = \frac{\alpha g \Delta T_B L^3}{\kappa v_1}. \tag{15}$$

This forced flow at the interface entrains by viscous coupling a thin sheet of the upper layer of thickness δ (as in the selective withdrawal problem, e.g. Lister 1989). Assuming that the viscous drag balances the buoyancy forces implies:

$$\alpha \Delta T_B g d - \frac{\Delta \rho}{\rho} g \delta \approx v_1 \frac{W_B}{d} \approx \frac{v_1 \kappa}{L^2} Ra_B^{2/5}. \tag{16}$$

Replacing d by its expression (16) finally gives

$$\delta \approx L \frac{\alpha \rho \Delta T_B}{\Delta \rho} Ra_B^{-1/5} \quad \text{at leading order.} \tag{17}$$

So far, the reasoning has been done in two-dimensions. To obtain the three-dimensional flux of entrained material, we assume that the 'sheet' extends a length L in the third dimension. The flux of material of layer 2 entrained in layer 1 is thus

$$Q_{21} = L \delta U_B \approx \kappa L \frac{\alpha \rho \Delta T_B}{\Delta \rho} Ra_B^{1/5} \tag{18}$$

Less viscous layer

The cylindrical plumes are steady on timescales (hours) much longer than the thermal instabilities in this layer (minutes), since they are centred on the top of the cells of the more viscous layer. They thus correspond to laminar plumes generated by a localized heat source. This situation has already been studied by Singer (1986) and Olson *et al.* (1993). Using a simplified boundary-layer model, they characterized the heat transport by a steady isoviscous axisymmetric cylindrical plume in an infinite Prandtl number fluid half-space above a heated surface. Their derivation leads to the following scaling laws:

$$\text{plume width} \quad \delta_p \approx a Ra^{-1/6}, \tag{19}$$

$$\text{centreline plume velocity} \quad W_p \approx \frac{\kappa}{a} Ra^{2/3}, \tag{20}$$

where a is the radius of the heat source and $Ra = \alpha g \Delta T_B a^3 / \kappa v_2$ is the plume Rayleigh number. These laws were found to be in good agreement with three-dimensional numerical results.

Arguments similar to those used for the more viscous layer show that the thickness of the entrained material schlieren is:

$$\delta_e \approx a \frac{\alpha \rho \Delta T_B}{\Delta \rho} Ra^{-1/6}, \tag{21}$$

and the flux of the material of layer 1 entrained in layer 2 by this cylindrical plume is:

$$Q_{12} = \delta_e^2 W_p \approx \kappa a \left(\frac{\alpha \rho \Delta T_B}{\Delta \rho} \right)^2 Ra^{1/3}. \tag{22}$$

Three unknowns remain in the problem: the horizontal interfacial temperature heterogeneity ΔT_B, the viscous cell half-width L, and the cylindrical plume heat source radius a. According to figure 8, the amplitude ΔT_B of the temperature heterogeneity at the interface is proportional to the total temperature difference ΔT applied across

the tank. Thus, I choose $\Delta T_B = \Delta T$. Since a plume is centred on top of each cell, the two lengthscales a and L must be closely related, i.e. $a = f(L)$. However, the lack of horizontal temperature profiles through the tank prevents complete determination of the function f. As a working hypothesis, I therefore assume the simplest form for f, i.e. that the two lengthscales are proportional. The number of cells, and their horizontal extent, does not change significantly during an experiment even though the depths of both layers are changing. So we choose as characteristic lengthscale the initial depth of the most viscous layer h_0.

The volumetric fluxes of entrained material finally are:

$$Q_{12} = C_1 \kappa h_0 \left(\frac{\alpha \rho \Delta T}{\Delta \rho} \right)^2 Ra_2^{1/3}, \tag{23a}$$

$$Q_{21} = C_2 \kappa h_0 \left(\frac{\alpha \rho \Delta T}{\Delta \rho} \right) Ra_1^{1/5}, \tag{23b}$$

where C_1 and C_2 are constants to be determined from the experiments. Note that within a given experiment, Q_{12} and Q_{21} evolve through time since both the viscosities and the densities of the layers change as entrainment proceeds.

4.2. *Comparison with the experiments and discussion*

For each experiment, the volume fluxes of entrained material Q_{12} and Q_{21} were calculated through time from the measurements using equations (7) and (8), and normalized by the scalings given by equations (23 a) and (23 b). Within the experiment, there is no systematic variation through time of the normalized volume flux and the scatter is consistent with the precision of the measurements. The scatter for the flux of entrained material in the less viscous layer is usually greater because the rate of change of ρ_2 is small compared to the accuracy of the measurements. The 'constants' (C_1, C_2) are defined as the mean values of the two normalized volume fluxes. Figure 16 shows C_1 and C_2 for all experiments as a function of the duration of the experiment. As expected, C_1 is more scattered than C_2, but each set is fairly coherent.

Although diffusion of NaCl is much slower in the Natrosol aqueous solutions used here than in pure water, owing to the increase in viscosity (see Appendix A), its influence is important under certain conditions. Accordingly, the experimental data define three different regimes of mass transport depending upon the Rayleigh numbers Ra_i, the buoyancy ratio R_ρ and the Lewis number Le. The last is difficult to estimate precisely because of the dependence of the salt diffusivity on Natrosol content. However, since diffusion at the interface always occurs, another mechanism can only take over if it can entrain material faster than salt diffuses. Now the length of an experiment will vary inversely with the strength of this other mechanism. Therefore the longer the experiment, the more likely it is that salt diffusion at the interface is important – not only at the end but throughout the experiment. Hence, one can hope to see different regimes of mass transport as the total duration on the experiment increases. Upon closer inspection, two of those can indeed be seen on figure 16, for durations t_{end} smaller and greater than 2000 min. The third regime corresponds to experimental data that cannot fit in the diagram.

4.2.1. *Mechanical entrainment*

For $t_{end} \leqslant 2000$ min, no obvious trend remains. For those experiments, the measurements of dye and salt concentrations give similar densities, so that chemical diffusion
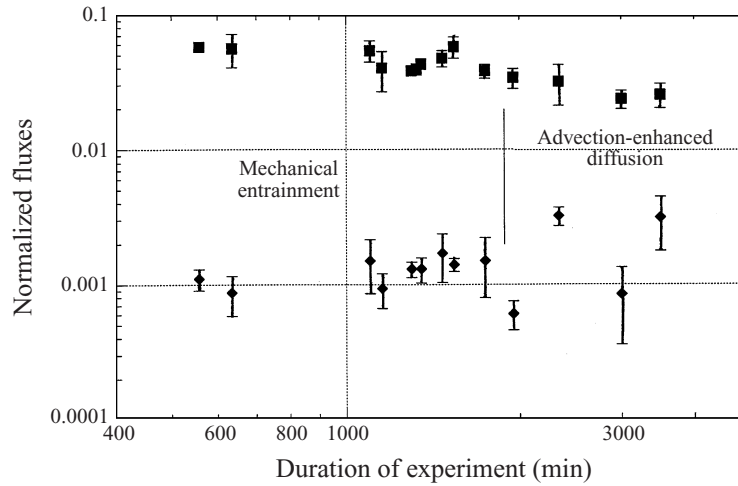
FIGURE 16. Time-average for each experiment of the normalized volume fluxes across the interface C_1 (diamonds) and C_2 (squares) as a function of the duration of the experiment (in min).

plays no role in the entrainment process. The mean values of the constants are then:

$$C_1 = 0.0012 \quad (\pm 32\,\%), \tag{24a}$$
$$C_2 = 0.0481 \quad (\pm 17\,\%). \tag{24b}$$

Using those constants in equations (23), one can then predict the complete time evolution of the system (densities and interface depth) for each experiment, by solving numerically the initial-value problem defined by equations (6)–(8) and (23) and the initial conditions of the experiment. This corresponds to the solid line on figures 12 and 13 for run 9.10. It compares very well with the measurements. This validates *a posteriori* the two main assumptions of the model, i.e. quasi-steady state and an entrainment scale (L) that does not change throughout the experiment.

4.2.2. *Advection-enhanced diffusion*

For $t_{end} \geqslant 2000$ min, the constant C_2 decreases with increasing duration, and the constant C_1 increases. During those four experiments, the density measurements based on salt and dye concentrations show small but systematic discrepancies (figure 17): the dye is transported across the interface more slowly than NaCl. However, the interface remains visually sharp, and the large temperature heterogeneities at the interface still exist. Hence, the mechanism that induces the large-scale entrainment remains the same and the volume fluxes of entrained material are still proportional to (23 a, b). This is a case of advection-enhanced diffusion (e.g. Solomon & Gollub 1988). Entrainment should also depend on the magnitude of the salt diffusion coefficient, but the uncertainty of its value in these experiments is too large to allow any trend in the results presented here to be deciphered. Moreover, the evolution of the viscosity of the layers through time was deduced from the salt measurements, assuming mechanical entrainment only. In the presence of salt diffusion, the values inferred by this method are therefore over-estimated for the upper layer and under-estimated for the lower layer. As a result, C_1 is over-estimated and C_2 under-estimated, as indeed can be observed in figure 16.
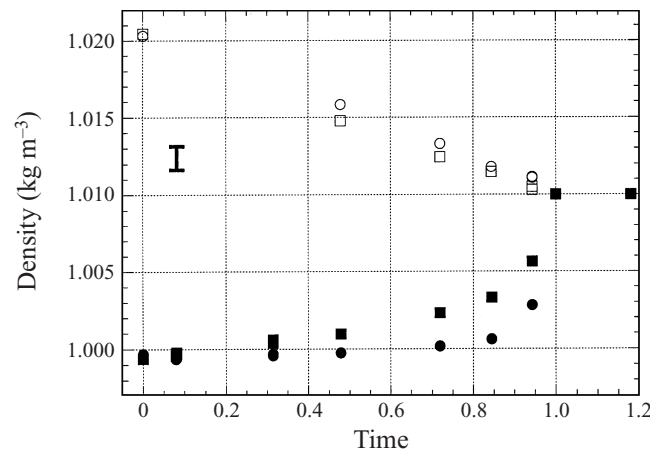
FIGURE 17. Run 4.30. Time evolution of the upper (black symbols) and lower (empty symbols) layers densities, deduced from the salt concentration (squares) and dye concentration (circles) measurements.

4.2.3. *Growth of a diffusive core*

Three experiments are not included in figure 16 since their behaviour neatly departed from what has been described so far. These experiments had in common a slowly moving (or even immobile) interface: (i) With no initial viscosity contrast between the two layers (run 8.40, table 1), and similar Rayleigh numbers, the interface remained at its initial depth and thickened with time. Soon, the sharp limit (as expressed visually by the colour and refraction index differences) between the two convecting layers was replaced by a diffuse stagnant layer and the convecting layers were pushed back towards the solid boundaries, both convection and entrainment becoming more sluggish. (ii) For large viscosity ratios and low Rayleigh numbers (run 8.50 and 8.90, table 1), the slow motions in the more viscous layer died out after some time, choked by the chemical diffusion of the material it had entrained. The remaining layer continued to convect and entrain salted material but failed to maintain a sharp interface or erode the non-convecting layer. Instead, the interface grew in size and became diffuse, confining convection towards the solid boundary. This convection eventually died out. In those three experiments, mechanical entrainment is slow compared to the diffusion of salt, so that double-diffusive effects govern the dynamics of the system, and a diffusive core grows at the interface as already described for low Prandtl number (e.g. Linden & Shirtcliffe 1973; Newell 1984; Fernando 1989).

5. Concluding remarks

This experimental study has shown that the possibility of entrainment in two-layer convection gives rise to a new interfacial instability, degenerating into cusps trough which all the mixing between the two layers proceeds. The classical mechanism of entrainment by turbulent eddies is not directly relevant for such laminar flows, as already noted by Solomon & Gollub (1988), but viscous stresses (Olson 1984) generated by interfacial lateral thermal gradients provide an adequate mechanism. A simple model of entrainment has been proposed and scaling laws derived that explain most of the entrainment data.

However, a number of uncertainties remain. In particular, what is the precise origin of the instability at the interface? At low buoyancy ratio, linear stability analysis
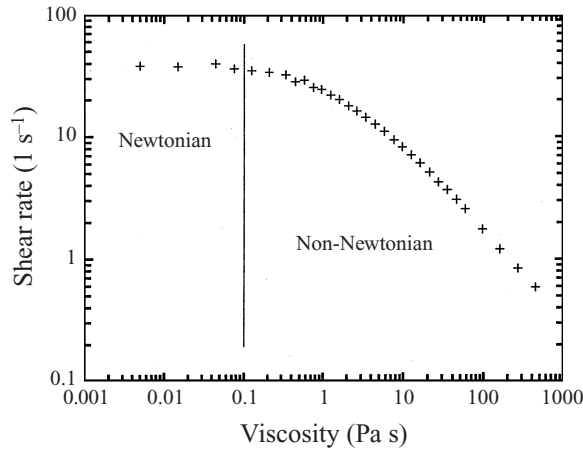
FIGURE 18. Viscosity as a function of shear rate (rotating viscometer). Aqueous solution with 1 % by wt Natrosol.

shows that it is probably the finite-amplitude expression of the oscillatory instability of the interface (Davaille 1998). However, at high buoyancy ratio and high Rayleigh number, the question is more difficult to answer. How large is the influence of diffusion? Three different regimes have been described but to draw a regime diagram would require experiments with other diffusing species. How is the global heat flux affected by the entrained chemical heterogeneities? An answer to this last question could help to understand better the energetics of laminar entrainment, especially the contribution of the interfacial viscous forces to the energy balance. Finally, I have focused on the entrainment mechanism only, adopting a global formalism to obtain quantitative predictions. This provides no insight into the fine structure of laminar mixing (for a review, see e.g. Ottino 1989). Clearly, two-layer thermal convection in miscible fluids deserves more work, both theoretical and experimental.

Appendix A. Physical properties of the fluids

Dynamic viscosity (η) measurements were made with a falling ball viscometer and a rotating viscometer over a range of shear rates at 23 °C. The solutions containing Natrosol are non-Newtonian, even for small quantities of Natrosol (figure 18). How-
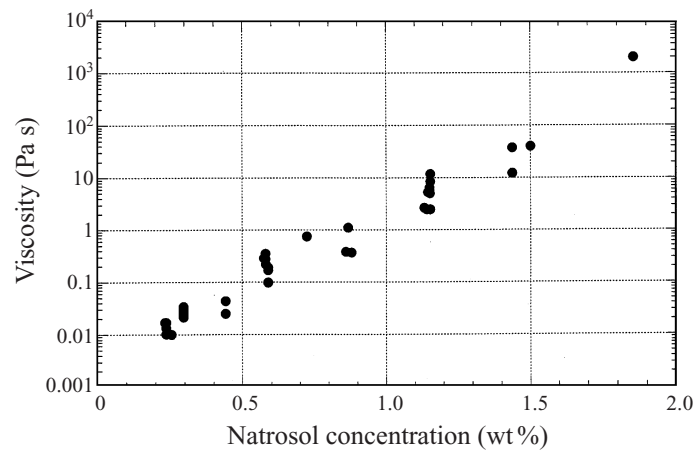
FIGURE 19. Newtonian viscosity (measured at low shear rates with a falling ball viscometer) of the experimental solutions as a function of the Natrosol concentration.

ever, for shear rates lower than $10^{-1}\,\mathrm{s}^{-1}$, the measured viscosity reached a plateau. For this range of shear rates, the values obtained with the falling ball viscometer (for descent times around 10 min) and the rotative viscometer agree. Moreover, the convective motions in the experiments were always slow enough that I could consider the viscosity of the fluids as Newtonian and equal to the value given by the falling ball viscometer measurement. Figure 19 shows the variation of the viscosity as a function of the percentage in weight of Natrosol in solution for all the solutions prepared. The dependence is approximately exponential. For a given experiment, knowing the initial densities ρ_{i0} and viscosities η_{i0} of the two layers, the viscosity η of a given layer at a given time can therefore be described by the following law:

$$\eta = \eta_{20} \exp\left(-\frac{\log(\eta_{10}/\eta_{20})}{(\rho_{10} - \rho_{20})}(\rho - \rho_{20})\right). \tag{A1}$$

The density ρ and dynamic viscosity η of both layers were measured at the beginning and at the end of each experiment, using floating densimeters and a falling ball viscometer. The kinematic viscosity $v = \eta/\rho$ was then calculated. Since Natrosol does not alter the thermal expansion coefficient (C. Jaupart, private communication), I used the law given by Ruddick & Shirtcliffe (1979) to calculate the coefficient of thermal expansion α of the solutions as a function of temperature and salinity.

The dependence of the chemical diffusion coefficients D (for salt or dye) on the Natrosol content is more difficult to estimate. According to the Stokes–Einstein equation (e.g. Bird *et al.* 1966), D depends mainly on the mobility of the molecules of the diffusing species and thus on the viscosity of the solute η and the radius of the diffusing particle R:

$$D \propto \frac{1}{\mu R}. \tag{A2}$$

Together with equation (A 1), this leads to an exponential dependence of the diffusion coefficient on the Natrosol content, a result which is well established for polymers. Moreover, across the interface between two layers of different viscosities, chemical diffusion will be limited by the more viscous layer. So, according to table 1 and equation (A 2), the salt diffusion coefficient in the solutions used here is estimated
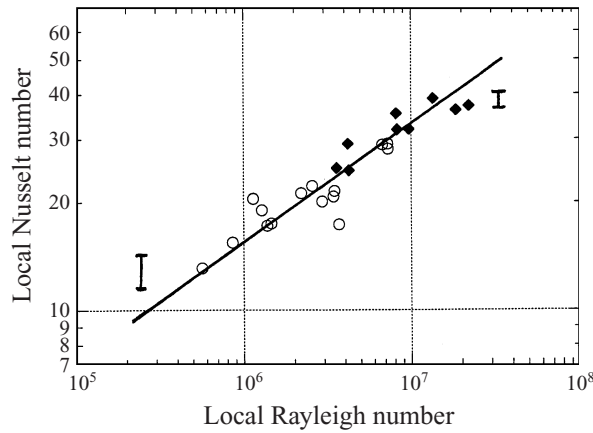
FIGURE 20. Local Nusselt number as a function of the local Rayleigh number for the classical one-layer Rayleigh–Bénard convection at the end of each experiment. The empty circles stand for the upper boundary layer, and the black diamonds for the lower boundary layer. The solid line has a slope of $\frac{1}{3}$.

to be between 10 and 10^6 times smaller than the salt diffusion coefficient in pure water ($= 1.6 \times 10^{-9}\,\mathrm{m}^2\,\mathrm{s}^{-1}$, Handbook of Chemistry and Physics, 1995). Since the dye molecules are bigger than the salt molecules, we expect the dye to diffuse even less than the salt, which was indeed observed.

Appendix B. High-Rayleigh-number thermal convection in viscous fluids

At each time t, the vertical temperature profiles were fitted by cubic splines and the heat fluxes were calculated in each thermal boundary layer:

$$Qs_1 = k\frac{\partial T}{\partial z}(z = 0), \quad Qs_2 = k\frac{\partial T}{\partial z}(z = H). \tag{B 1}$$

For the classical one-layer Rayleigh–Bénard regime at the end of each experiment, to calculate the local heat fluxes at two different locations by moving around the thermocouples probe gives the same value: ergodicity was verified. The main uncertainty on the heat fluxes comes from the uncertainty on the depths of the thermocouples ($\pm 0.25\,\mathrm{mm}$). It leads to a uncertainty of 10 (for low Rayleigh numbers when there are at least three thermocouples in the boundary layer) to 50 % (for high Rayleigh numbers when there are only two thermocouples in the boundary layer). In figure 20, the data with an error greater than 30 % have been discarded.

At high Rayleigh number, the instability neechanism is expected to be independent of the depth of the layer (Howard 1964). This leads to equation (3) for the onset time of convection, which agrees well with the experimental data (figure 2, Blair & Quinn 1969; Kaviany 1980; Davaille & Jaupart 1994). For the heat flux in the well-developed convective regime, it gives:

$$Nu = \frac{Qs}{k\dfrac{(T_m - T_i)}{H}} = CRa_m^b \quad b = \tfrac{1}{3}, \tag{B 2}$$

where T_m is the temperature of the well-mixed interior, C an experimental constant and Ra_m, the local Rayleigh number based on the physical properties of the boundary

layer $Ra_m = \alpha_i g(T_m - T_i)H^3/\kappa v$. When inertial effects are important (e.g. in water, air or helium), laboratory experiments have shown that this relation breaks down for Rayleigh numbers greater than 4×10^7 (e.g. Castaing *et al.* 1989) with an exponent b closer to $\frac{2}{7}$. However, for high-Prandtl-number fluids, (B 2) has been found experimentally to hold at least up to $Ra \sim 10^9$ (Goldstein, Chiang & See 1990; Guillou & Jaupart 1995). In the present case, the thermal expansion coefficient depending strongly on temperature, the local Nusselt number and the local Rayleigh number for the top and bottom boundaries were calculated using the thermal expansion coefficients corresponding to the temperature of each boundary. Although the uncertainty on the data cannot rule out a lower exponent b, figure 20 shows that the data is compatible with equation (B 2), and gives a constant $C = 0.15$.

The conservation of heat through the tank and equation (B 2) can also be used to calculate the temperature of the well-mixed interior T_m: when all the physical properties are equal in the two boundary layers, T_m is the mean of the boundary temperatures $T_{1/2}$. However, when the thermal expansion coefficient depends on temperature, it is given by:

$$T_m = T_1 - \Delta T \frac{(\alpha_2/\alpha_1)^{1/4}}{1 + (\alpha_2/\alpha_1)^{1/4}}. \tag{B 3}$$

Equation (B 3) explains well the discrepancy (which can reach 25 %) between the measured T_m and $T_{1/2}$ shown in figure 6 and observed in all experiments.

REFERENCES

ASAEDA, T. & WATANABE, K. 1989 The mechanism of heat transport in thermal convection at high Rayleigh numbers. *Phys. Fluids* A **1**, 861–867.

BEARDSLEY, R. C. & FESTA. J. F. 1972 A numerical model of convection driven by a surface stress and non-uniform heating. *J. Phys. Oceanogr.* **2**, 444–455.

BIRD, R. B., STEWART, W. E. & LIGHTFOOT, E. N. 1966 *Transport Phenomena*. Wiley.

BLAIR, L. M. & QUINN, J. A. 1969 The onset of cellular convection in a fluid layer with time-dependent density gradients. *J. Fluid Mech.* **36**, 385–400.

BOSS, A. P. & SACKS, I. S. 1986 High spatial resolution models of time-dependent, layered convection. *Geophys. J. R. Astron. Soc.* **87**, 241–264.

BUSSE, F. H. 1981 On the aspect ratios of two-layer mantle convection. *Phys. Earth Planet. Inter.* **24**, 320–324.

CASTAING, B., GUNARATNE, G., HESLOT, F., KADANOF, L., LIBCHABER, A., THOMAS, S. & WU, X.-Z. 1989 Scaling of hard turbulence in Rayleigh–Bénard convection. *J. Fluid Mech.* **204**, 1–30.

CHRISTENSEN, U. 1980 Numerical experiments on convection in a chemically layered mantle. *J. Geophys. Res.* **49**, 82–84.

CHRISTENSEN, U. & YUEN, D. A. 1984 The interaction of a subducting slab with a chemical or phase boundary. *J. Geophys. Res.* **89**, 4389–4402.

CHU, T. Y. & GOLDSTEIN, R. J. 1965 Turbulent convection in a horizontal layer of water. *J. Fluid Mech.* **60**, 141–159.

CSEREPES, L. & RABINOWICZ, M. 1985 Gravity and convection in a two-layered mantle. *Earth Planet. Sci. Lett.* **76**, 193–207.

CSEREPES, L., RABINOWICZ, M. & ROSEMBERG-BOROT, C. 1988 Three-dimensional infinite Prandtl number convection in one and two layers with implications for the Earth's gravity field. *J. Geophys. Res.* **93**, 12009–12025.

DAVAILLE, A. 1998 Thermal convection in two superimposed miscible fluids with different viscosities. Part I: linear stability analysis.

DAVAILLE, A. & JAUPART, C. 1993 Transient high-Rayleigh-number convection with large viscosity variations. *J. Fluid Mech.* **253**, 141–166.

DAVAILLE, A. & JAUPART, C. 1994 Onset of thermal convection in fluids with temperature-dependent viscosity: application to the oceanic mantle. *J. Geophys. Res.* **99**, 19853–19866.

DEARDORFF, J. W., WILLIS, G. E. & LILLY, D. K. 1969 Laboratory investigation of non-steady penetrative convection. *J. Fluid Mech.* **35**, 7–31.

ELLSWORTH, K. & SCHUBERT, G. 1988 Numerical models of thermally and mechanically coupled two-layered convection in highly viscous fluids. *Geophys. J.* **93**, 347–363.

FERNANDO, H. J. S. 1989 Buoyancy transfer across a diffusive interface. *J. Fluid Mech.* **209**, 1–34.

FERNANDO, H. J. S. 1991 Turbulent mixing in stratified fluids. *Ann. Rev. Fluid Mech.* **23**, 455–493.

GOLDSTEIN, R. J., CHIANG, H. D. & SEE, D. L. 1990 High Rayleigh-number convection in a horizontal enclosure. *J. Fluid Mech.* **213**, 111–126.

GUILLOU, L. & JAUPART, C. 1995 On the effect of continents on mantle convection. *J. Geophys. Res.* **100**, 24217–24238.

HOWARD, L. N. 1964 Convection at high Rayleigh number, In *Proc. 11th Intl Congr. Applied Mechanics* (ed. H. Görtler), pp. 1109–1115. Springer, Berlin.

HUPPERT, H. E., SPARKS, R. S. & TURNER, J. S. 1984 Some effects of viscosity on the dynamics of replenished magma chambers. *J. Geophys. Res.* **89**, 6857–6877.

JARVIS, G. T. & PELTIER, W. R. 1982 Mantle convection as a boundary layer phenomenon. *Geophys. J. R. Astron. Soc.* **68**, 389–427.

JEONG, J.-T. & MOFFATT, H. K. 1992 Free-surface cusps associated with flow at low Reynolds number. *J. Fluid Mech.* **241**, 1–22.

JOSEPH, D. D., NELSON, J., RENARDY, M. & RENARDY, Y. 1991 Two-dimensional cusped interfaces. *J. Fluid Mech.* **223**, 383–409.

JOSEPH, D. D. & RENARDY, M. 1993 *Fundamentals of Two-Fluids Dynamics*. Springer, New York, pp. 443.

KAVIANY, M. 1980 The onset of thermal convection in a fluid layer subjected to transient heating from below. *J. Heat Transfer* **106**, 817–823.

KENYON, P. M. & TURCOTTE, D. L. 1983 Convection in a two-layer mantle with a strongly temperature-dependent viscosity. *J. Geophys. Res.* **88**, 6403–6414.

KRISHNAMURTI, R. 1970 On the transition to turbulent convection. *J. Fluid Mech.* **42**, 295–320.

LINDEN, P. F. & SHIRTCLIFFE, T. G. L. 1978 The diffusive interface in double-diffusive convection. *J. Fluid Mech.* **87**, 417–423.

LISTER, J. R. 1989 Selective withdrawal from a viscous two-layer sytem. *J. Fluid Mech.* **198**, 231–254.

NATAF, H.-C., MORENO, S. & CARDIN, P. 1988 What is responsible for thermal coupling in layered convection? *J. Phys. France* **49**, 1707–1714.

NEWELL, T. A. 1984 Characteristics of a double diffusive interface at high density stability ratios. *J. Fluid Mech.* **149**, 385–401.

OLSON, P. 1984 An experimental approach to thermal convection in a two-layered mantle. *J. Geophys. Res.* **89**, 11293–11301.

OLSON, P., SILVER, P. G. & CARLSON, R. W. 1990 The large scale structure of convection in the Earth's mantle. *Nature* **344**, 209–215.

OLSON, P., SCHUBERT, G. & ANDERSON, C. 1993 Structure of axisymmetric mantles plumes. *J. Geophys. Res.* **98**, 6829–6844.

PELLEW, A. & SOUTHWELL, R. V. 1940 On maintained convective motion in a fluid heated from below. *Proc. R. Soc. Lond.* A **176**, 312–343.

PROCTOR, M. R. E. & JONES, C. A. 1988 The interaction of two spatially resonant patterns in thermal convection. Part 1. Exact 1:2 resonance. *J. Fluid Mech.* **188**, 301–355.

OTTINO, J. M. 1989 The Kinematics of Mixing: Stretching, Chaos, and Transport. Cambridge University Press, 364 pp.

RASENAT, S., BUSSE, F. H. & REHBERG, I. 1989 A theoretical and experimental study of double-layer convection. *J. Fluid Mech.* **199**, 519–540.

RENARDY, Y. & JOSEPH, D. D. 1985 Oscillatory instability in a Bénard problem of two fluids. *Phys. Fluids* **28**, 788–793.

RENARDY, Y. & JOSEPH, D. D. 1985 Perturbation analysis of steady and oscillatory onset in a Bénard problem with two similar liquids. *Phys. Fluids* **28**, 2699–2708.

RENARDY, M. & RENARDY, Y. 1985 Perturbation analysis of steady and oscillatory onset in a Bénard problem with two similar liquids. *Phys. Fluids* **28**, 2699–2708.

RICHTER, F. M. & JOHNSON, C. E. 1974 Stability of a chemically layered mantle. *J. Geophys. Res.* **79**, 1635–1639.

RICHTER, F. M. & MCKENZIE, D. P. 1981 On some consequences and possible causes of layered convection. *J. Geophys. Res.* **86**, 6133–6124.

ROSSBY, H. T. 1965 On thermal convection driven by non-uniform heating from below: an experimental study. *Deep-Sea Res.* **12**, 9–16.

RUDDICK, B. R. & SHIRTCLIFFE, T. G. L. 1979 Data for double-diffusers: physical properties of aqueous salt-sugar solutions. *Deep-Sea Res.* **26**, 775–787.

SCHMITT, R. W. 1994 Double diffusive oceanography. *Ann. Rev. Fluid Mech.* **26**, 255–285.

SINGER, H. A. 1986 Heat transport by steady state plumes with strongly temperature-dependent viscosity. PhD thesis. The Johns Hopkins University, Baltimore, MD, 196 pp.

SOLOMON, T. H. & GOLLUB, J. P. 1988 Passive transport in Steady Rayleigh–Bénard Convection. *Phys. Fluids* **31**, 1372–1379.

SOTIN, C. & PARMENTIER, E. M. 1989 On the stability of a fluid layer containing a univariant phase transition: application to planetary interiors. *Phys. Earth Planet. Inter.* **55**, 10–25.

TAIT, S. & JAUPART, C. 1989 Compositional convection in viscous melts. *Nature* **338**, 571–574.

TURNER, J. S. 1979 *Buoyancy Effects in Fluids*. Cambridge University Press. 368 pp.